Flow-induced vibrations of a tethered circular cylinder

K. Ryan*, C.J. Pregnalato, M.C. Thompson, K. Hourigan

Fluids Laboratory for Aeronautical and Industrial Research (FLAIR), Department of Mechanical Engineering, Monash University, Melbourne, Victoria 3800, Australia

Abstract

One of the most basic examples of fluid-structure interaction is provided by a tethered body in a fluid flow. The tendency of a tethered buoy to oscillate when excited by waves is a well-known phenomenon; however, it has only recently been found that a submerged buoy will act in a similar fashion when exposed to a uniform flow at moderate Reynolds numbers, with a transverse peak-to-peak amplitude of approximately two diameters over a wide range of velocities. This paper presents results for the related problem of two-dimensional simulations of the flow past a tethered cylinder. The coupled Navier–Stokes equations and the equations of motion of the cylinder are solved using a spectral-element method. The response of the tethered cylinder system was found to be strongly influenced by the mean layover angle as this parameter determined if the oscillations would be dominated by in-line oscillations, transverse oscillations or a combination of the two. Three branches of oscillation are noted, an in-line branch, a transition branch and a transverse branch. Within the transition branch, the cylinder oscillates at the shedding frequency and modulates the drag force such that the drag signal is dominated by the lift frequency. It is found that the mean amplitude response is greatest at high reduced velocities, i.e., when the cylinder is oscillating predominantly transverse to the fluid flow. Furthermore, the oscillation frequency is synchronized to the vortex shedding frequency of a stationary cylinder, except at very high reduced velocities. Visualizations of the pressure and vorticity in the wake reveal the mechanisms behind the motion of the cylinder.

1. Introduction

As an extension to the case of the flow-induced vibration of a hydroelastically mounted cylinder in a uniform flow field, a study has been performed on the flow-induced vibration of a buoyant tethered cylinder. This system geometry has practical applications in submerged pipelines, ocean spars, and tethered lighter-than-air craft. It is also of interest as it exhibits flow-induced oscillation where the combined effects of in-line oscillation and transverse oscillation may be observed. Finally, both numerically and analytically, the tethered cylinder provides a simplification to the fully three-dimensional problem of a tethered sphere, which has been the subject of recent investigation (Govardhan and Williamson, 1997; Williamson and Govardhan, 1997; Jauvtis et al., 2001).

Most previous work regarding tethered bodies has focused on the free surface interaction with tethered buoys (Harlemann and Shapiro, 1961; Shi-Igai and Kono, 1969; Ogihara, 1988). In each of these studies, the tethered bodies

*Corresponding author. IRPHE, Technopole de Chateau Gombert, 49 rue Joliot Curie—B.P. 146, Marseille, Cedex 13384, France. Tel.: +33 4 96139775; fax: +33 4 96139709.

E-mail address: Kris.Ryan@irphe.univ-mrs.fr (K. Ryan).

oscillate due to the combined effect of a uniform (or sheared) free stream and free surface wave effects. This combination, incorporating the interaction of a free surface, has made interpretation of results complex and conclusions difficult to draw.

To date, little research has been performed concerning fully submerged tethered bluff bodies and only the related work of Williamson and Govardhan (1997), Govardhan and Williamson (1997), and Jauvtis et al. (2001) deal purely with the action of a tethered sphere in a uniform flow. For tethered spheres with low mass ratio ($m^* < 1$, where m^* is the ratio of the body density to the fluid density), the experimental investigation of Williamson and Govardhan (1997) found that large amplitude oscillations occurred. They found that the tethered sphere sustained large peak-to-peak oscillations with amplitudes of the order of two sphere diameters in the transverse direction. They also found smaller stream-wise oscillations of the order of about 0.4 sphere diameters. Their work was extended by Jauvtis et al. (2001) to incorporate spheres with higher mass ratios, $m^* > 1$. In this study, four branches of shedding were observed, two of which were observed for a sphere with $m^* < 1$.

The vortex-induced vibration of tethered bodies is a component of the more general area of flow-induced vibration of bluff bodies. Most work in this area has centered on the flow-induced vibration of a hydroelastically mounted cylinder. Two critical parameters have been identified in these studies, namely the mass-damping parameter, $m^*\zeta$, and the reduced velocity, $u^* = u/f_n D$ (where ζ is the mechanical damping coefficient, f_n is the natural frequency of the tethered body system, and D is a characteristic body length and is generally chosen as the diameter for a circular cylinder). Traditionally, these studies have focused on high mass ratio, ($m^* \gg 1$) hydroelastically mounted cylinders with a high mechanical damping coefficient, ζ. However, more recent investigations have focused on low $m^*\zeta$, and their findings are relevant to the present study; the mass ratio investigated in this study is less than unity, and the tether provides effectively no mechanical damping.

Khalak and Williamson (1999), in their investigation of a low mass-damped cylinder, found a lock-in regime occurred where the cylinder oscillated transverse to the free-stream at the vortex shedding frequency of the wake. Within this lock-in regime, three distinct branches of cylinder oscillation were observed as the flow speed was increased: an initial, upper and lower branch of oscillation. Govardhan and Williamson (2000), Blackburn et al. (2001) and Shiels et al. (2001) have also found these three branches of oscillation for low mass-damped cylinders. The lock-in regime has been observed for higher $m^*\zeta$ cylinders, however only two of the observed branches appear to exist, namely the initial and lower branch (Bearman, 1984; Parkinson, 1989).

Govardhan and Williamson (2000) found that the upper branch exhibited significantly higher amplitude oscillations than either of the other two branches. They also found that the upper and lower branches exhibit a '2P' wake structure, where two vortex pairs are shed per oscillation cycle. They found that transition from the upper to the lower branch results in a change of the phase between the total lift force and the cylinder displacement; the upper branch exhibiting in-phase oscillation, the lower branch of oscillation exhibiting 180° out-of-phase oscillation. Further, they found that when oscillation amplitude was plotted against u^*, the transition point from the upper to the lower branch of shedding was inversely proportional to the mass ratio of the cylinder. They postulated that, for a cylinder mass ratio less than 0.54, the upper branch of shedding, and hence the lock-in regime, continues indefinitely for increasing reduced velocities. Recent experiments performed by Govardhan and Williamson (2003) have confirmed this.

Also of note is the dependence of the frequency of vortex-induced oscillation on the mass ratio (m^*) of the body. For cylinders of a high mass ratio, the vibration frequency tends to the natural frequency of the cylinder [for example, Feng (1968)]. However, experiments by Angrilli et al. (1974) found that for cylinders with a low mass ratio ($m^* \simeq 1.5$), the vibration frequency tended toward the vortex shedding frequency of the flow.

It is anticipated that, at large mean lay-over angles (see Fig. 1 for a definition of the mean layover angle, θ), the tethered cylinder will behave in a fashion similar to the low mass-damped hydroelastically mounted cylinder and should oscillate in either the upper or lower branch of shedding depending on the reduced velocity and the mass ratio.

In this study, m^* was chosen to be 0.833 and the tether length ratio (the length of the tether normalized against the cylinder diameter), L^*, was chosen as 5.05. These values were selected to match experiments conducted simultaneously in the FLAIR water channel. Preliminary results from the water channel experiments were used to validate the present results describing the cylinder mean layover angle. The reduced velocity was taken as the controlling parameter and was varied between $1 \leqslant u^* \leqslant 22$. Two distinct peaks in the oscillation amplitude were observed. A small peak at $u^* = 2.5$, where the cylinder was observed to oscillate predominantly in-line with the flow direction, and a much larger peak at $u^* = 20$, where the cylinder was oscillating primarily transverse to the flow direction.

In Section 2, the equations that are to be solved are presented, and in Section 3 the numerical technique is described and the results of grid resolution studies are presented. The results of the study are presented and discussed in Section 4.

2. Problem formulation

The coordinate system and geometry of the problem are shown in Fig. 1. For the purpose of illustration, a body of arbitrary geometry is considered without loss of generality. Note that θ is the mean layover angle formed by the plane of the tether to the y-axis and ϕ is the instantaneous angle of oscillation about θ. The values of θ and ϕ are not known *a priori*, however, an initial instantaneous angle $(\theta + \phi)$ is predicted at the start of a given simulation. The forces acting on the object are composed of hydrodynamic loading (drag and lift) and the tension in the tether. The buoyancy of the body (B) is combined with the pressure and viscous lift to give a net vertical force, and is denoted by $F_L + B$ in Fig. 1.

We consider the flow of a viscous incompressible fluid past a tethered cylinder. The equations representing this problem are the coupled system of fluid and bluff body equations. The Navier–Stokes equations governing the fluid motion in an inertial reference frame are given by

$$\frac{\partial \mathbf{u}'}{\partial t} + (\mathbf{u}' \cdot \nabla')\mathbf{u}' = -\nabla' p' + \frac{1}{\mathrm{Re}}\nabla'^2 \mathbf{u}', \tag{1}$$

$$\nabla' \cdot \mathbf{u}' = 0, \tag{2}$$

in which $\mathbf{u}'$ is the velocity field normalized by the inlet velocity (U), p' is the static pressure normalized by $(\rho_w U^2)$, where ρ_w is the fluid density, t is time normalized by the nondimensional time D/U, where D is the cylinder diameter, and $\mathrm{Re} = UD\rho_w/\mu$ is the Reynolds number. (Note: the prime indicates variables are taken relative to the inertial reference frame.)

The tether is assumed to be rigid and inextensible (i.e., no radial or flexure movement). The coefficient of tension per unit length within the tether is given by

$$C_T = C_D \sin(\theta + \phi) + (C_L + \alpha(1 - m^*))\cos(\theta + \phi), \tag{3}$$

where C_D and C_L are the drag and lift coefficients and θ and ϕ are defined in Fig. 1.

The acceleration of the structure is a result of the forces acting on it and can be calculated from

$$\frac{\pi}{2} m^* \ddot{x}' = C_D - C_T \sin(\theta + \phi), \tag{4}$$

$$\frac{\pi}{2} m^* \ddot{y}' = (C_L + \alpha(1 - m^*)) - C_T \cos(\theta + \phi). \tag{5}$$

Combining Eqs. (3), (4) and (5) results in the following equations for the components of the acceleration of the cylinder in Cartesian form:

$$\ddot{x}' = \frac{1}{L^{*2}m^*}[C_D y'^2 - (C_L + (1 - m^*)\alpha)x'y'], \tag{6}$$

$$\ddot{y}' = -\frac{1}{L^{*2}m^*}[C_D y'x' - (C_L + \alpha(1 - m^*))x'^2], \tag{7}$$

where $\alpha = \pi g D/2u^2 = \pi/2Fr^2$, and x' and y' are both nondimensional and have been normalized by D.

In general, the vector body force coefficient per unit length C_f (defining the lift and drag coefficients) is computed by integrating the pressure and viscous stress terms as

$$C_f = 2 \oint \left(-p\mathbf{n} + \frac{1}{\mathrm{Re}}(\nabla \mathbf{u} + \nabla \mathbf{u}^{\mathrm{T}}) \cdot \mathbf{n}\right)\mathrm{d}s, \tag{8}$$

where the integration is performed over the entire surface of the cylinder and $\mathbf{n}$ is the outward unit normal vector to the surface. As C_D and C_L are calculated directly from Eq. (8), they include all the fluid forces acting on the cylinder and no added mass term is required in Eqs. (4) and (5).

3. Methodology

Solving fluid-structure interaction problems generally involves the use of deforming and/or moving meshes. Fig. 2 shows the transformation used to map the inertial reference frame to the time-independent reference frame. This mapping is described by
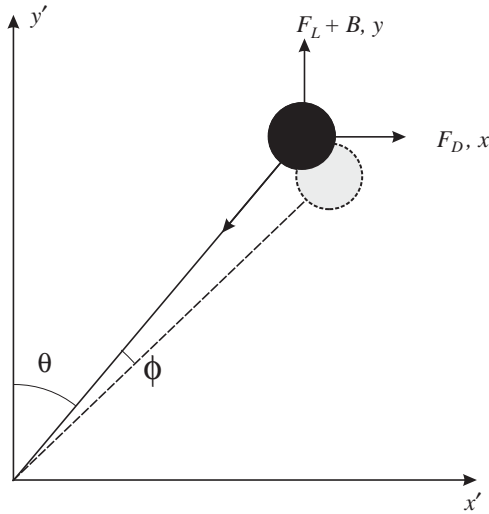
$$\mathbf{x} = \mathbf{x}' - \mathbf{X}(t), \tag{9}$$

Fig. 1. Idealized schematic of the tethered cylinder in fluid flow. The tethered cylinder has a mean layover angle from the vertical, θ, and a oscillation angle about this mean layover angle, ϕ.
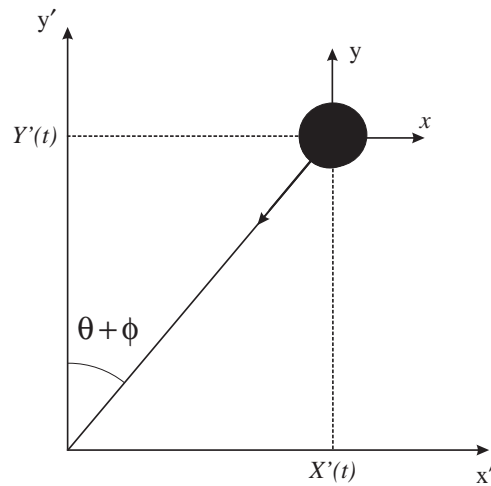

Fig. 2. Schematic of the transformation used to map from inertial to noninertial reference frame. The simulations are conducted with respect to the cylinder.

where $X(t)$ is the normalized displacement of the cylinder and is described in terms of $\theta + \phi$ as

$$X(t) = L^* \sin(\theta + \phi(t)), \quad Y(t) = L^* \cos(\theta + \phi(t)). \tag{10}$$

In the transformed system of coordinates, the center of the cylinder is stationary, although it is free to rotate. Given the transformation (9), Eqs. (1) and (2) become

$$\frac{\partial \boldsymbol{u}}{\partial t} + (\boldsymbol{u} \cdot \boldsymbol{\nabla})\boldsymbol{u} = -\boldsymbol{\nabla} p + \frac{1}{\mathrm{Re}} \, \nabla^2 \boldsymbol{u} + A^*, \tag{11}$$

$$\boldsymbol{\nabla} \cdot \boldsymbol{u} = 0, \tag{12}$$

where the forcing term A^* is an additional dimensionless acceleration term introduced by the noninertial coordinate transformation, Eq. (9), and is the acceleration of the cylinder given by Eqs. (6) and (7), normalized by U^2/D. Due to

the attachment of the coordinate system to the cylinder, the cylinder will rotate as it moves about the base pivot. Hence, the boundary conditions need to be altered in order to account for this effect.

The equations of motion for the fluid and the cylinder are discretized in space using a spectral-element method. Typically, eighth-order Lagrangian polynomials were used as the tensor-product expansion basis. Eqs. (6) and (7) governing the body's motion, are solved using a predictor–corrector technique. The Navier–Stokes and continuity equations, Eqs. (9) and (10), are discretized in time using a three-step time-splitting approach [see Karniadakis et al. (1991) for further details]. The acceleration term A^* is combined with the nonlinear terms and these are treated in the first substep of the time update.

The coupled fluid/structure equations are solved in three steps. First, an initial angle θ is set (corresponding to an initial displacement x_0) and the fluid equations are solved. Next, the drag, lift and side forces are computed using Eq. (8). Finally, the structural motion is updated using Eqs. (6) and (7) and the process is repeated.

A plot of the two-dimensional mesh is shown in Fig. 3. The mesh consists of $\kappa = 518$ macro-elements. The inlet length, defined as the distance between the inlet and the cylinder surface is $l_i = 14.5D$. Owing to the mesh geometry, the cross-flow width is the same as the inlet length. The outlet length is $l_o = 24.5D$.

Detailed resolution tests were performed on a stationary cylinder to verify grid independence. A Reynolds number value of 500 was chosen for two reasons; first, it represents the highest Reynolds number considered for this (and other) investigations and therefore represents the most rigorous grid resolution study possible; secondly, the grid resolution results may be compared against the findings of Blackburn and Henderson (1999) in their numerical study, where their grid resolution study was conducted at the same Reynolds number. The order of the interpolating polynomials was increased from $N = 5$ to 9. Flow quantities such as the Strouhal number, lift and drag coefficients were measured and compared to previous values published in the literature. The results are summarized in Table 1. For all measures employed, the variation between the values at $N = 7$ and 9 is less than 1%. Furthermore, the values of all measures for $N = 8$ (used in all subsequent simulations) compare to within 1% of the numerical values of Blackburn and Henderson (1999), and Henderson (1995). Mesh independence was also verified for the moving cylinder by considering the two extremes of tether angle; at small angles, motion was predominantly in the cross-flow direction, whereas at large angles, the motion was largely in the stream-wise direction. For each value of N from 5 to 10, mean tether angles, oscillation amplitudes, oscillation frequencies, and drag and lift coefficients were measured for these two extreme cases. Again, all quantities compare to within 1% for the $N = 8$ case.

Simulation results for the flow past a fixed cylinder at Re = 200 were also compared with the two-dimensional numerical findings of Zhang and Dalton (1998), and Henderson (1995). In this case, the Strouhal number, mean drag and peak lift coefficients were compared with previous findings. The results are presented in Table 2. The current results compare favorably with previous findings. The largest deviation across the three sets of results was for the mean drag coefficient results, where the present results were found to be 2.9% and 1.5% greater than the results of Zhang and Dalton (1998) and Henderson (1995), respectively. The present results for both the Strouhal number and peak lift coefficient were found to vary by less than 2% when compared to the results reported by Zhang and Dalton (1998).

Experimentally, the reduced velocity, u^*, is altered by changing the inlet velocity, hence Re is linearly dependent on u^*. However, for the simulations discussed in this paper the Reynolds number was held fixed at Re = 200. A fixed Reynolds number allows the study of the effect of the reduced velocity, u^*, in isolation, without including the effect of changed flow field diffusion between simulations. Also, if the inlet velocity were the controlling parameter, the linear dependence of Re with u^* would reduce the applicability of results from two-dimensional numerical simulations to model the flow.

The choice of Re = 200 was made as it is the highest Reynolds number that can be justifiably simulated using a two-dimensional model. Beyond this Reynolds number, experimental and numerical investigations indicate that three-dimensional structures in the wake of a stationary cylinder act to alter the wake characteristics when compared to the results obtained from two-dimensional simulations (Williamson, 1996). Large amplitude oscillations act to increase the correlation length along the span of a cylinder, suggesting that two-dimensional simulations of these systems may be used to study higher Reynolds number flows [for example, Blackburn and Henderson (1999)]. However, Koopman (1967), in his investigation of forced cylinder oscillation, found that Re = 200 is the highest Reynolds number with a two-dimensional field regardless of the amplitude of oscillation.

When considering the flow past a fixed cylinder, both the mean drag coefficient and the Strouhal number remain relatively constant in the range $200 \leqslant \mathrm{Re} \leqslant 10\,000$. However, within this range, both the formation length and the ratio of viscous to pressure drag terms vary. Clearly, these discrepancies will lead to differences in the body-fluid interaction between the numerical results and the experimental results; in particular, the amplitude of cylinder oscillation may be affected by the ratio of viscous to pressure drag terms.

The numerical results describing the mean layover angle were compared against results from preliminary experiments conducted in the FLAIR water channel. This facility has a 4 m long test section which is 0.6 m in width and 0.8 m in
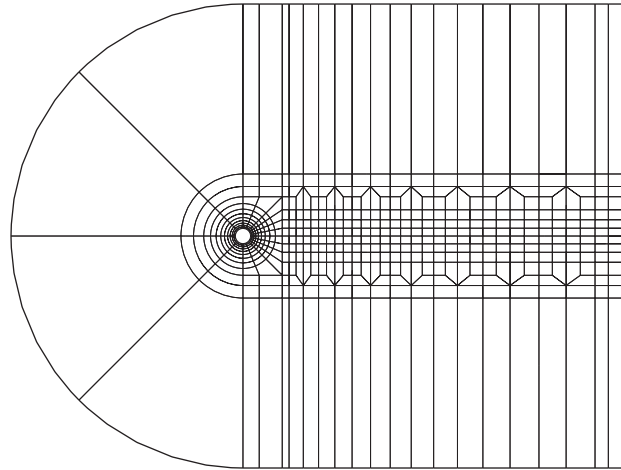
Fig. 3. Macro-element mesh used for the simulations.

Table 1
Convergence results for a stationary cylinder at Re = 500

N	5	6	7	8	9
$C_{L(P)}$	1.19	1.18	1.18	1.18	1.18
$C_{D(P)}$	1.59	1.58	1.58	1.58	1.58
$C_{D(m)}$	1.46	1.45	1.45	1.45	1.45
St	0.23	0.23	0.23	0.23	0.23

The symbol (p) denotes peak values, (m) denotes mean values.

Table 2
Convergence results for a stationary cylinder at Re = 200

	St	$C_{L(P)}$	$C_{D(m)}$
Current results	0.199	0.69	1.36
Zhang and Dalton (1998)	0.198	0.68	1.32
Henderson (1995)			1.34

The symbol (p) denotes peak values, (m) denotes mean values.

depth measured from the free surface to the channel floor. The cylinder diameter was 25 mm and the cylinder span to diameter ratio was $L_S : D = 17 : 1$. Reynolds numbers in the range Re = 1000–3500 were investigated.

4. Results

The cylinder studied was of fixed mass ratio and tether length. The cylinder response in terms of oscillation amplitude, fluid dynamic forces and oscillation frequency as a function of u^* were predicted. In this study, the mass ratio (m^*) was chosen to be 0.833 and the normalized tether length ($L^* = L/D$) was chosen as 5.05. As mentioned previously, these values were selected to match preliminary experiments conducted simultaneously in the FLAIR water channel.

Following the work of Govardhan and Williamson (1997), Williamson and Govardhan (1997), and Jauvtis et al. (2001), results are presented as a function of reduced velocity ($u^* = u/f_n D$) which incorporates the inlet velocity,

cylinder diameter and natural frequency of the system. Note that the natural frequency of the system is a function of the tension in the tether and varies with the drag, lift and buoyancy, unlike that of a hydroelastically mounted cylinder which is independent of hydrodynamic forces.

Since the problem is essentially that of a pendulum with external forcing applied, the natural frequency is given by

$$f_n = \frac{1}{2\pi} \sqrt{\frac{\overline{T}}{mL}}, \tag{13}$$

where $\overline{T}$ is the mean tension force acting through the tether averaged across a motion cycle, m is the mass of the cylinder, and L is the tether length. The mean tension can be decomposed in terms of the drag and buoyancy forces, and written in nondimensional form as

$$\overline{C_T} = \frac{\overline{T}}{\frac{1}{2}\rho_w U^2 D} = \sqrt{\overline{C_D}^2 + [\alpha(1 - m^*)]^2}. \tag{14}$$

By substituting Eqs. (13) and (14) into the definition for the reduced velocity, and rewriting in nondimensional form, we obtain

$$u^* = \frac{2\pi^{\frac{3}{2}}}{\sqrt{2}} \left(\frac{(m^* + C_a)L^*}{\left(\overline{C_D}^2 + [\alpha(1 - m^*)]^2\right)^{1/2}} \right)^{1/2}, \tag{15}$$

where C_a is the added mass coefficient [see Govardhan and Williamson (2000) for details], and is equal to 1 for a circular cylinder. The parameter α was varied between $0.8 \leqslant \alpha \leqslant 1500$ (corresponding to normalized velocities of $1 \leqslant u^* \leqslant 22$).

For mean layover angles, θ, less than approximately $30°$, Eq. (15) may be simplified by neglecting the mean drag coefficient, as the buoyancy force dominates drag force in this layover range. If this simplification is made, Eq. (15) reduces to the same form as that found by Williamson and Govardhan (1997) describing the reduced velocity for the flow past a tethered sphere.

4.1. Mean layover angle results

Fig. 4 shows the mean layover angle obtained through the numerical simulations, as well as results from the water channel experiments, both as a function of reduced velocity. The numerical simulations are found to closely match the experimental values for $u^* < 12$. Valid results from the experimental rig were limited to this reduced velocity range [corresponding to a Reynolds number range of (Re = 1000–3500)]; for $u^* > 12$, the mean layover angle was such that the boundary layer on the channel base interfered with both the cylinder motion and the hydrodynamic forces acting on the cylinder. The mean drag acting on cylinder was not measured directly in experiments. Instead, by assuming the mean lift tended to zero, the drag may be determined from the mean layover angle from

$$\theta = \tan^{-1}\left(\frac{C_D}{(1 - m^*)\alpha} \right). \tag{16}$$

An analytical estimate of the mean lay-over angle was also made from Eq. (16) and is plotted in Fig. 4 as a solid line. Here, the drag coefficient was held constant ($C_D = 1.34$), and was equal to the drag coefficient for a stationary cylinder at the corresponding Reynolds number of Re = 200 (Henderson, 1995). For $u^* < 5$, the predicted response using Eq. (16) describes both the numerical and experimental values of θ accurately. In the reduced velocity range, $5 < u^* \leqslant 18.5$, the rate of increase of θ with respect to u^* gradually deviates away from the predicted curve. Beyond $u^* = 18.5$ this rate of increase rapidly diminishes and crosses the predicted curve at $u^* \simeq 20$. Beyond $u^* = 20$, the curve overpredicts θ. Eq. (16) is essentially the ratio of drag to buoyancy force. Assuming constant buoyancy for a given mass ratio, any deviation in θ away from that predicted from Eq. (16) implies a variation in the drag force away from that found for a fixed circular cylinder. For a given u^*, $\theta_{\text{numerical}} > \theta_{\text{predicted}}$ implies that the mean drag is greater than that of a fixed cylinder and $\theta_{\text{numerical}} < \theta_{\text{predicted}}$ implies that the mean drag is less than that of a fixed cylinder.

The drag coefficient is presented in Fig. 5 as a function of u^*. As anticipated from the previous discussion, the drag coefficient gradually increases from that of a fixed cylinder in the range $5 < u^* < 18.5$ before rapidly decreasing below
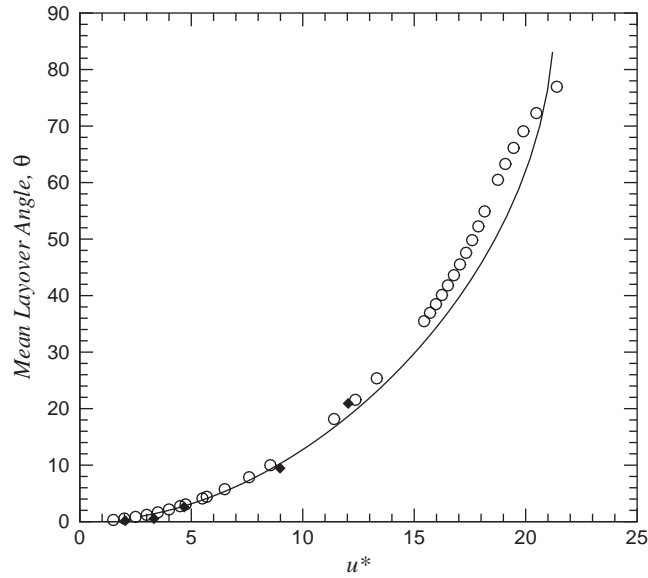
Fig. 4. Mean layover angle, θ, as a function of reduced velocity, u^*: $\bigcirc$, numerical simulation; $\blacklozenge$, experimental results; $-$, analytical estimate (note the analytical estimate assumes a fixed $C_D = 1.34$, which is equivalent to the drag coefficient for the flow past a fixed cylinder at a Reynolds number of 200).
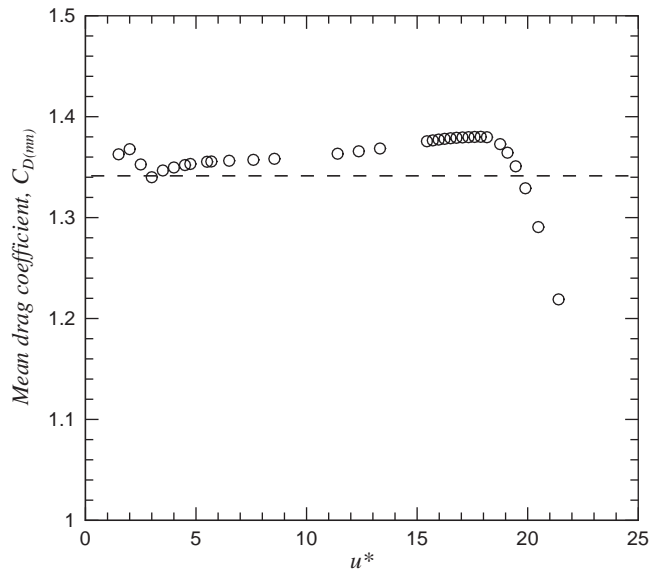

Fig. 5. Mean drag coefficient, C_D, as a function of reduced velocity, u^*: $\bigcirc$, numerical simulation of tethered cylinder; $--$, for the flow past a fixed cylinder at a Reynolds number of 200.

that of a fixed cylinder for $u^* > 19$. A small peak is observed at $u^* = 2.5$. At these low layover angles, the buoyancy force dominates the drag force and predictions using Eq. (16) accurately estimate θ. Any variation in the drag may be associated with an increased amplitude in the oscillation of the tethered cylinder. Fig. 5 indicates that two local maxima in the oscillation amplitude should be observed at $u^* = 2.5$ and 19. The small deviation in the mean drag as a function of reduced velocity indicates that the cylinder oscillations should be small for the entire range of reduced velocity investigated.

4.2. Amplitude of oscillation

The normalized amplitude of oscillation in the direction of cylinder motion ($A^* = A/D$) is presented in Fig. 6 along with the in-line ($x^* = x/D$) and transverse ($y^* = y/D$) components, each as a function of the reduced velocity. As anticipated, two distinct peaks are observed in A^*; the first, occurring at $u^* = 2.5$, is very small in amplitude and is dominated almost entirely by the in-line component. This dominance implies that the forcing is comprised almost entirely of the drag force component. It appears that the peak is due to a resonance between the natural frequency, f_n, of the system and the drag signal, f_D, which (at this reduced velocity) is twice the lift frequency, f_L. Assuming the Strouhal number is St $\simeq 0.2$, the natural frequency and the drag signal are equivalent at $u^* \simeq 2.5$, in agreement with the assumption of a resonance between the two frequencies.

The peak amplitude of the oscillations at $u^* = 2.5$ (dominated by an in-line component) is far lower than the second peak found at $u^* = 19$ (dominated by a transverse component). The relative amplitudes of the in-line and transverse branches is in agreement with King (1974), who studied the in-line vortex-induced oscillation of a hydroelastically mounted cylinder. He found two in-line branches of oscillation in the reduced velocity range, $u^* \simeq 1$–3 with a maximum in-line oscillations peaking at $A^* = 0.12D$. He found that the first branch has a symmetric shedding wake, while the wake structure of the second branch resembles a Karman vortex street.

At a reduced velocity, $u^* = 17$, corresponding to a mean lay-over angle, $\theta = 45°$, the transverse component of oscillation, y^*, begins to dominate the in-line component. The in-line component of oscillation peaks at $u^* = 17.5$ prior to decreasing rapidly. Throughout the reduced velocity range, $u^* = 5$–19, A^* continues to increase and is increasingly dominated by the transverse component.

A second peak in A^* is observed at a reduced velocity of $u^* \simeq 20$. At this reduced velocity, the mean lay-over angle is $\theta \simeq 70°$, and the oscillations are dominated by the transverse component (y^*), which accounts for 93% of the oscillation amplitude in the direction of motion. For reduced velocities greater than 20, both A^* and y^* decrease rapidly with u^*. At these high layover angles, the cylinder behaves in a fashion similar to a low mass-damped, hydroelastically mounted cylinder undergoing transverse vortex-induced vibration as described by Khalak and Williamson (1999) and Govardhan and Williamson (2000). The high value of u^*, combined with $m^* = 0.833$, implies that the oscillations occur on the lower branch of oscillation and that the cylinder oscillations become desynchronized from the vortex shedding frequency. At $u^* = 22$, this phenomenon is observed, the oscillation time series is chaotic and appears uncorrelated to the vortex shedding frequency. The cylinder oscillation at these high reduced velocities ($u^* > 20$) is therefore in agreement with the findings of Govardhan and Williamson (2000).

Three force coefficients can be identified that describe the transient forces acting on the cylinder to induce motion; the drag coefficient, C_D, the lift coefficient, C_L, and the force coefficient acting in the direction of motion, C_{Tan}. The
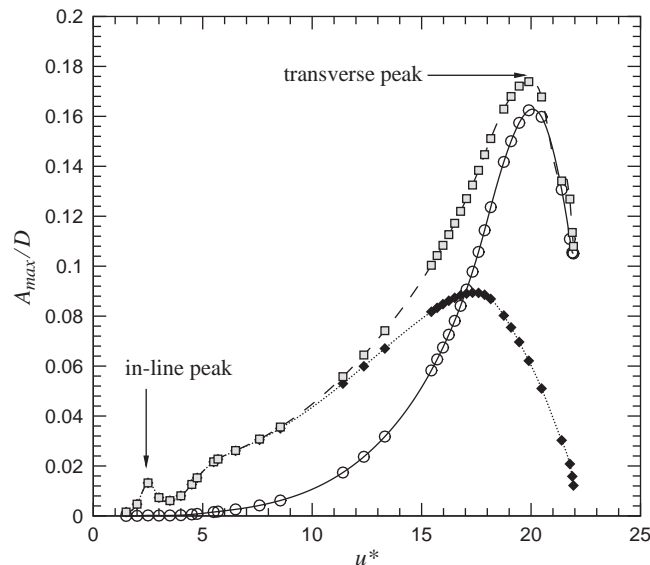

Fig. 6. Normalized amplitude of oscillation as a function of reduced velocity: ◆, in-line component of normalized oscillation amplitude; ◯, transverse component of normalized oscillation amplitude; □, normalized oscillation amplitude in the direction of motion.

instantaneous value of C_{Tan} is defined by

$$C_{\text{Tan}} = C_D \cos(\theta + \phi) - (C_L + \alpha(1 - m^*)) \sin(\theta + \phi). \tag{17}$$

A plot of the r.m.s. values of the amplitudes of each of these coefficients is presented in Fig. 7, as a function of the reduced velocity. In the reduced velocity range, $u^* = 1$–4, all three r.m.s. force coefficients exhibit significant fluctuations. As anticipated, both $C_{D,\text{rms}}$ and $C_{\text{Tan,rms}}$ exhibit a local peak at $u^* = 2.5$. Of interest is $C_{D,\text{rms}}$, whose peak value at $u^* = 2.5$ is larger in amplitude than r.m.s. C_{Tan}. By considering the mean layover angle at this reduced velocity ($\theta = 0.875°$), it would be assumed that the cylinder oscillates in the in-line direction, and the oscillations are almost entirely independent of the fluctuating lift force. This is clearly not the case, and Eq. (17) indicates that the instantaneous amplitude of the lift force is considerably greater than the instantaneous amplitude of the drag force, and acts to reduce the total force contribution in the direction of motion. From Fig. 7, this is indeed the case; $C_{L,\text{rms}}$ is over five times that of the $C_{D,\text{rms}}$. As with the in-line amplitude of motion, $C_{D,\text{rms}}$ peaks at $u^* \simeq 17.5$ before decaying. The value of $C_{\text{Tan,rms}}$ peaks at $u^* \simeq 19$ before decaying, its maximum value barely exceeds the maximum drag value. For $u^* > 20$, the $C_{L,\text{rms}}$ dominates the $C_{\text{Tan,rms}}$ and both decay up to the highest reduced velocity investigated.

4.3. Frequency of oscillation

Fig. 8 shows the fundamental frequency of oscillation, normalized against the natural frequency of the tethered cylinder system, as a function of the reduced velocity. In this figure, the solid line is the Strouhal number for a fixed cylinder (St_1), corresponding to the fixed cylinder lift frequency, and the dashed line is twice the Strouhal number of the shedding frequency for a fixed cylinder (St_2), corresponding to the fixed cylinder drag signal.

For $u^* < 5$, the principal frequency of oscillation is synchronized with St_2, i.e., the in-line force frequency for a fixed cylinder. This is anticipated as the cylinder is restricted to oscillate in the in-line direction. At $u^* \simeq 2.5$, St_2 is synchronized with the natural frequency of the tethered body system, accounting for the peak in both the oscillation amplitude and the r.m.s. in-line force at this reduced velocity (Figs. 6 and 7).

In the reduced velocity range, $u^* = 2.5$–3.5, there is a reduction in the oscillation amplitude and r.m.s. fluid forces (see Figs. 6 and 7). This is due to the oscillation frequency no longer being synchronized with the natural frequency of the tethered cylinder system. From Fig. 6, the oscillation amplitude increases rapidly with increasing reduced velocity in the range $u^* = 3.5$–5. At $u^* = 5$, St_1 is synchronous with the natural frequency of the system and the dominant oscillation frequency switches to St_1. Beyond $u^* = 5$, as the oscillation frequency departs from f_n, there is a sudden decrease in the gradient of oscillation amplitude as a function of reduced velocity (as shown in Fig. 6), however the dominant oscillation frequency remains close to St_1.

Only two regions of synchronization or "lock-in" are found when one considers the classical definition of lock-in, i.e., a synchronization of the vortex shedding frequency (f_V) and body oscillation frequency (f) with the natural frequency of the system (f_n), so that $f^* = f/f_n$ is close to unity, which is valid for hydroelastically mounted cylinders of large $m^* = \mathcal{O}(100)$. The first, at $u^* = 2.5$, results in a local peak of the oscillation amplitude, the second at $u^* = 5$ results in a change in gradient in the oscillation amplitude vs u^*. If the ratio between the fluid forcing frequency and the shedding frequency from a fixed cylinder is considered (Govardhan and Williamson, 2000), a lock-in regime clearly exists for a much broader range of $u^* = 1$–19. This form of lock-in behavior is similar to the response of a freely vibrating cylinder at very low mass-damping (Khalak and Williamson, 1999). This is in contrast with a low mass-ratio tethered sphere in which the oscillation frequency has been found not to correspond to either the vortex shedding frequency or natural frequency within the same reduced velocity range (Govardhan and Williamson, 1997).

The transition in the principal frequency from synchronization with St_2 to synchronization with St_1 would, at first glance, imply a transition in the dominant force component from drag to lift. However, this transition occurs at a surprisingly low reduced velocity when the mean layover angle is considered. At $u^* = 5$, the mean layover angle, $\theta = 4.2°$, and it would be assumed that the drag force would continue to dominate the oscillations in preference to the lift force. Analysis of Fig. 6 also implies that C_{Tan} is dominated by drag up to $u^* \simeq 17$, well beyond the point of frequency transition, and analysis of Fig. 7 clearly confirms this assumption. This leads to the conclusion that the drag signal is dominated by the same frequency as the lift for $u^* > 4$. As the reduced velocity increases beyond 17, the dominant driving force switches to the lift force; however, the frequency of oscillation does not change as the principal frequency of the lift remains equivalent to the principal frequency of the drag force.

The abrupt switch in dominant frequency at $u^* = 5$ is apparent in Fig. 9. For $u^* < 5$, the dominant normalized frequency, f_1, is 0.4 (or the drag signal) and the secondary normalized frequency, f_2, is 0.2 (the lift frequency). At $u^* = 5$, f_1 and f_2 switch values, such that for $u^* > 5$, f_1 is 0.2 and f_2 is 0.4. A decrease in both f_1 and f_2 of the cylinder oscillation is observed for $u^* > 19$ as the oscillations become desynchronized with the wake flow field.
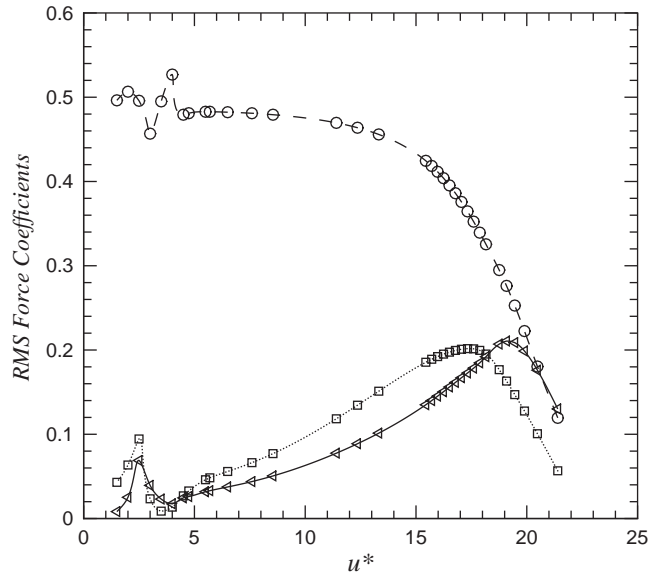
Fig. 7. R.m.s. force coefficients as a function of reduced velocity: $\bigcirc$, $C_{L,\text{rms}}$; $\square$, $C_{D,\text{rms}}$; $\triangleleft$, $C_{\text{Tan,rms}}$ (force coefficient in the direction of motion).
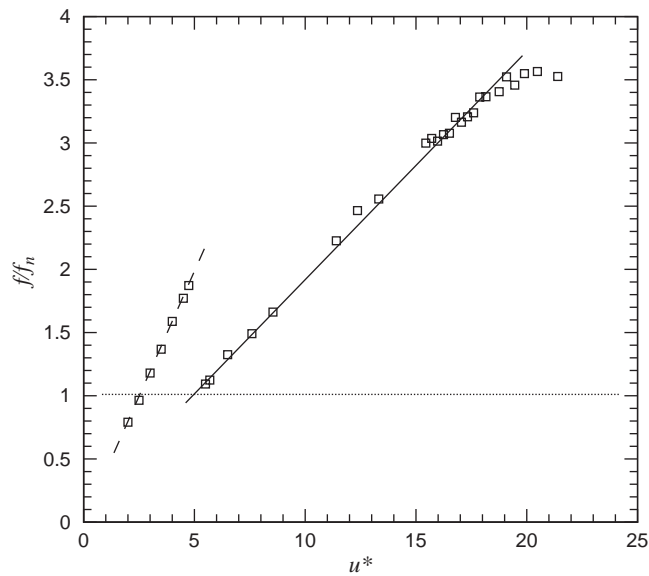

Fig. 8. Frequency of oscillation, normalized against the natural frequency of the tethered body system (f/f_n) as a function of the reduced velocity. The dashed line is the drag frequency for the flow past a fixed cylinder at a Reynolds number of 200; the solid line is the lift frequency for the flow past a fixed cylinder at a Reynolds number of 200.

4.4. Time history of oscillation

Three branches of oscillation have so far been discussed and are clearly visible in Figs. 6 and 7. The first branch ($u^* \simeq 2.5$) is due to a resonance between the drag signal and the natural frequency of the system. The second branch occurs in the reduced velocity range, $u^* = 5$–19, peaking at $u^* = 19$. In the previous section, it was hypothesized that the
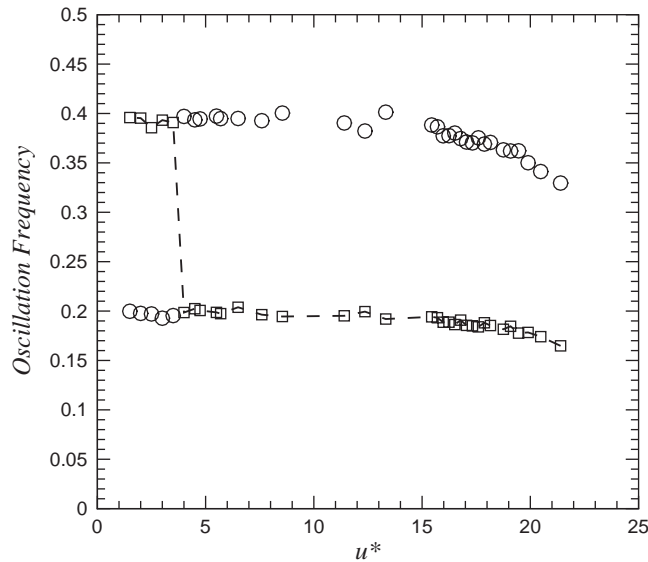
Fig. 9. Principal (f_1) and secondary (f_2) components of the cylinder oscillation as a function of reduced velocity. □, Principal frequency of oscillation; ○, secondary frequency of oscillation.

change in the oscillation frequency is due to a resonance between the natural frequency of the tethered body system and the subharmonic of the drag signal. For $u^* > 19$, the oscillations are dominated by the lift force, and the tethered cylinder appears to behave as a hydroelastically mounted cylinder.

Time histories of the fluid forces and cylinder motion for $u^* = 2.5, 3.5$ and 5.5 are presented in Figs. 10a, 10b and 10c, respectively. At $u^* = 2.5$, the drag signal clearly has twice the frequency of the lift signal, suggesting a Karman type wake shedding and indicating that the local peak in A^* observed at this reduced velocity compares with the second instability region of in-line oscillation observed by King (1974). Both C_{Tan} and A^* exhibit the same frequency as the drag force term with a slight modulation in amplitude due to the lift term.

As the reduced velocity is increased to 3.5, a significant alteration is observed. As anticipated, the drag force diminishes markedly in amplitude as the drag force is no longer synchronized with the natural frequency of the tethered cylinder system. However, every second peak of the drag signal is substantially greater in amplitude than the neighboring peaks. The normalized amplitude of oscillation (A^*) shows the same behavior, indicating that the natural frequency of the system is indeed influencing the subharmonic of the drag force.

As the reduced velocity is further increased to $u^* = 5.5$, the drag is clearly dominated by St_1 and is in phase with the lift. This may explain the increase in the amplitude of oscillation as both the r.m.s. lift and drag forces act in unison to drive the cylinder oscillations. Both A^* and C_{Tan} are also dominated by the St_1 frequency lending support to this theory.

Beyond $u^* = 19$, the drag signal remains dominated by St_1, however the St_2 component is more noticeable when compared to lower reduced velocities. The time history for $u^* = 22$ is presented in Fig. 10d. Every second drag peak has a higher amplitude then its neighboring peak indicating that a significant component of the St_1 frequency still exists in the drag signal. At this reduced velocity, the cylinder behaves similarly to a low mass-damped cylinder oscillating transverse to the flow field. The phase angle between the cylinder motion and C_{Tan} is $180°$. For a very low mass-damped freely oscillating cylinder (Govardhan and Williamson, 2000), the phase angle between the displacement and forcing was $180°$ only for the lower branch of amplitude response. This similarity provides an explanation for the reduction in A^* and the de-synchronization from the vortex shedding frequency for $u^* > 19$, as the cylinder is now oscillating in the lower branch of shedding as described by Govardhan and Williamson (2000) for a hydroelastically mounted cylinder.

Fig. 11 depicts the spectral density of the cylinder oscillation as a function of the reduced velocity. For $u^* \leqslant 5$, no peak is apparent for the St_1 frequency, and the St_2 frequency dominates the cylinder oscillations. For $u^* > 5$, a local peak in the frequency synchronous with the St_1 frequency is apparent. A local peak in the frequency synchronous with the St_2 frequency is observed for all reduced velocities studied.
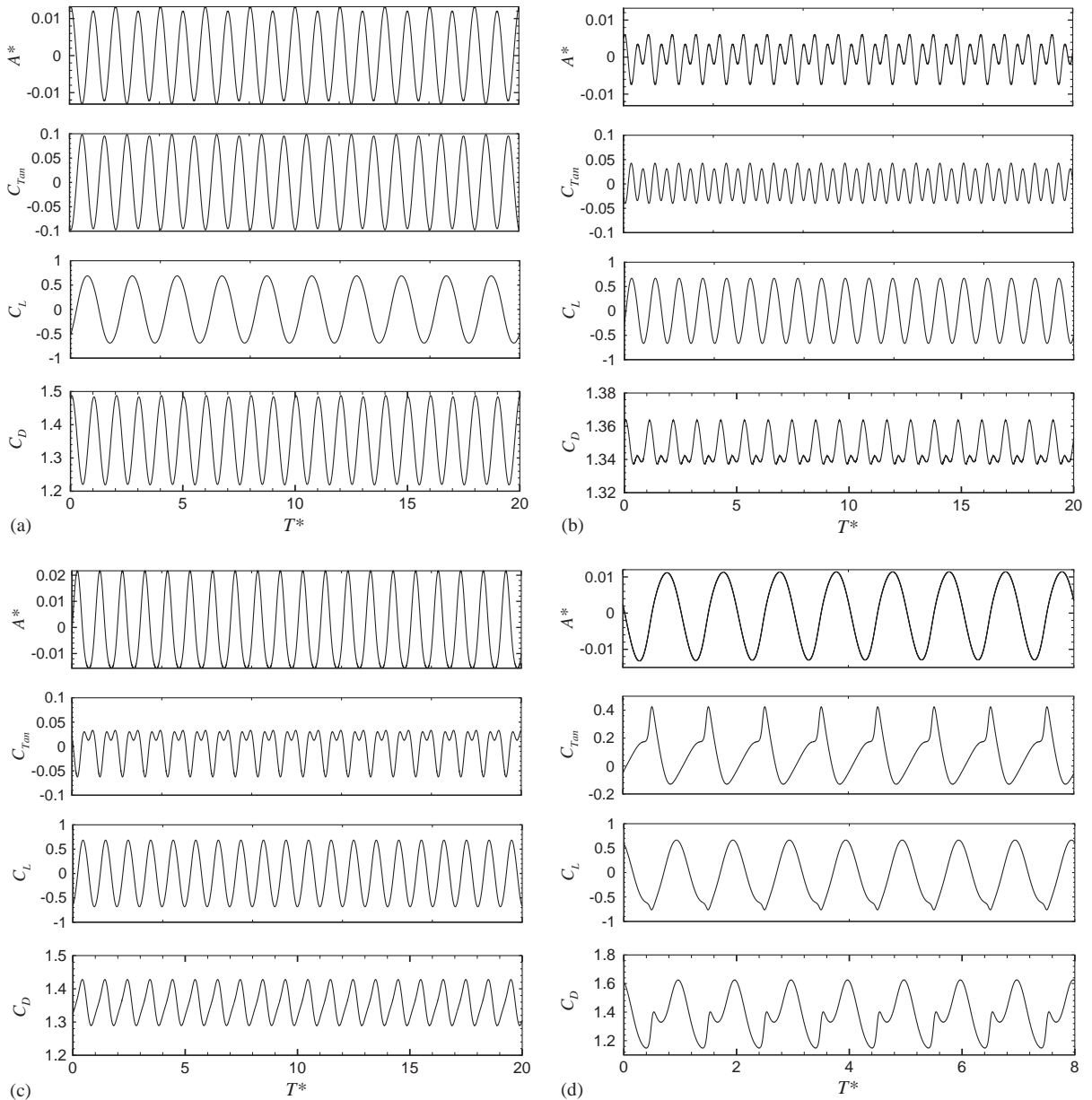
Fig. 10. (a) Variation of amplitude and force coefficients against normalized time for $u^* = 2.5$. (b) Variation of amplitude and force coefficients against normalized time for $u^* = 3.5$. (c) Variation of amplitude and force coefficients against normalized time for $u^* = 5.5$. (d) Variation of amplitude and force coefficients against normalized time for $u^* = 22$.

4.5. Flow field analysis

The transition from an St_2 to an St_1 dominated drag cycle may be better described by the analysis of pressure plots of the flow field over one period of the cylinder shedding cycle. Contour plots of the pressure fields are presented in Figs. 12a and 12b.

Fig. 12a shows the pressure field for a cylinder at the top of the cylinder cycle, defined as the uppermost position of the cylinder counter clockwise from the mean layover angle. The image on the left and right correspond to $u^* = 2.5$ and 5.5, respectively. The wake flow field is seen to be in-phase by comparing the two images.
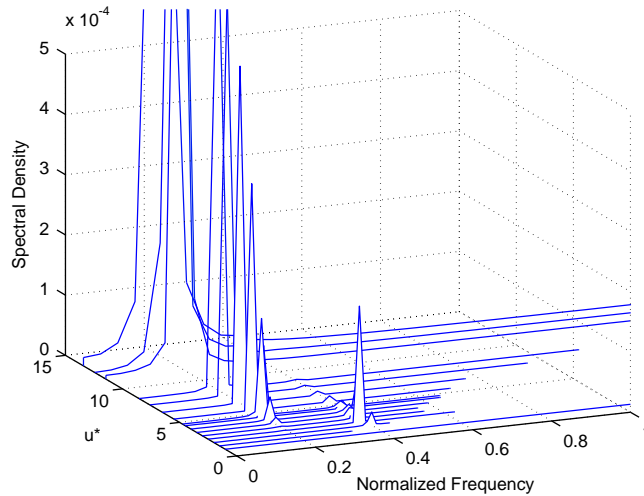
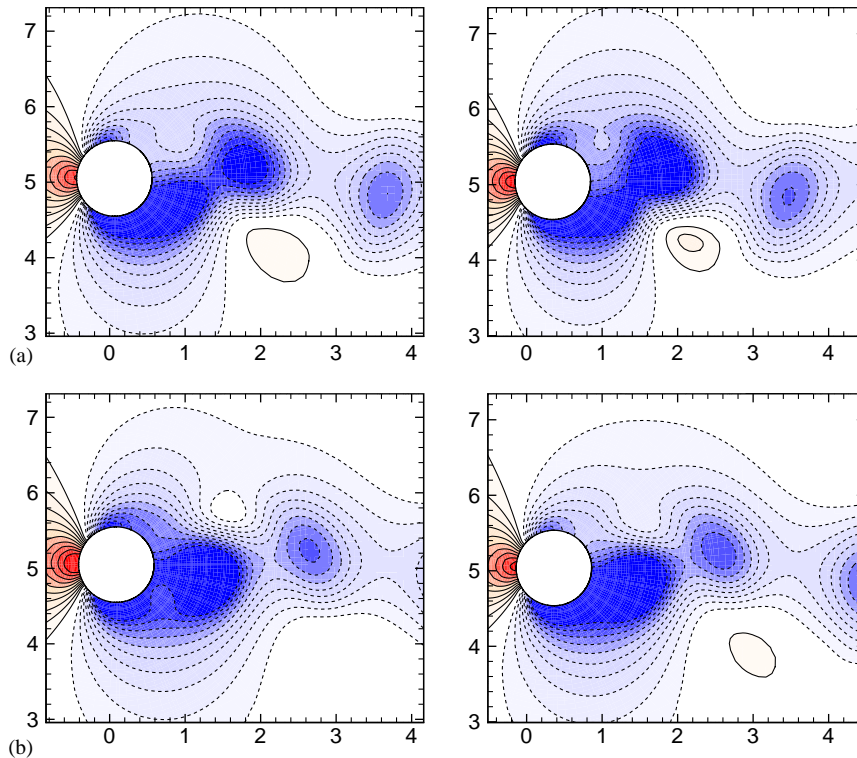Fig. 11. Spectral density of the cylinder oscillation as a function of reduced velocity.

Fig. 12. (a) Pressure coefficient contours about the tethered cylinder at (left) $u^* = 2.5$ and (right) $u^* = 5.5$ for the uppermost position (most counter-clockwise position from the mean layover angle) of the cylinder in its cycle. Contours are evenly spaced over the range (blue) $-0.5 \leqslant C_P \leqslant 0.5$ (red); with $\Delta C_P = 0.05$. (b) Pressure coefficient contours about the tethered cylinder at (left) $u^* = 2.5$ and (right) $u^* = 5.5$, one-quarter of a shedding cycle after the cylinder reaches its uppermost position. Contours are evenly spaced over the range (blue) $-0.5 \leqslant C_P \leqslant 0.5$ (red); with $\Delta C_P = 0.05$.

For both reduced velocities, the wake flow field is of the von Karman type. At this phase of the oscillation cycle, the drag coefficient is at its lowest point for both reduced velocities, and there are few differences between the two pressure fields.

Fig. 12b depicts the pressure flow field taken one-quarter of a shedding cycle later. In this case, the cylinder oscillating at $u^* = 2.5$ has reached the bottom of its cycle (i.e., it is halfway through its oscillation cycle) and is essentially stationary with respect to the pivot point. However, the cylinder oscillating at $u^* = 5.5$ is only one-quarter through its oscillation cycle and is moving in the flow field direction with a maximum velocity with respect to the pivot point. As with Fig. 12a, the wake pressure fields for both the reduced velocities are remarkably similar, however the stagnation pressure acting at the front of the cylinder for $u^* = 2.5$ is significantly greater than for $u^* = 5.5$. It would appear that the motion of the cylinder, oscillating at its natural frequency at $u^* = 5.5$, reduces the intensity of the stagnation pressure point over half of its cycle providing a drag signal component at the cylinder oscillation frequency (St_1). The drag cycle retains a component of the St_2 frequency due to the Karman type shedding wake for the entire range of reduced velocities investigated. The St_1 frequency is simply superimposed over this for $u^* > 3.5$.

Time histories of the base pressure coefficient (C_{PB}) and the leading-edge pressure coefficient (C_{PLE}) for $u^* = 2.5$ and $u^* = 5.5$ are shown in Figs. 13a and 13b. As may be observed in Fig. 13a, both C_{PB} and C_{PLE} are synchronized with the St_2 frequency. As the reduced velocity is increased to $u^* = 5.5$ (Fig. 13b), C_{PB} remains dominated by the St_2 frequency, however the St_1 frequency is also apparent. By contrast, C_{PLE} is dominated by the St_1 frequency, in a fashion similar to the drag signal at this reduced velocity.

At higher reduced velocities, the cylinder oscillation remains synchronized with the lift frequency (St_1) and sufficient horizontal motion is retained to reduce the pressure at the leading edge stagnation point over half the oscillation cycle up to a reduced velocity of $u^* = 19$. Beyond $u^* = 19$, the cylinder's horizontal motion is less dominant as the cylinder oscillates principally in the transverse direction, and the dominant drag signal reverts to St_2 for these high reduced velocities.

Fig. 14 depicts the vorticity field for a cylinder oscillating at a reduced velocity $u^* = 22$ at the top of its oscillation cycle. Here, the cylinder is oscillating principally in the transverse direction ($\theta = 79°$) and is behaving as a low mass-damped hydroelastically mounted cylinder oscillating in the lower branch.

Of interest is that the shedding into the wake is clearly a 2S branch of shedding, as is the shedding for all reduced velocities investigated. This finding is especially relevant at this high reduced velocity as it is in contrast with the experimental findings of Govardhan and Williamson (2000), who found 2P shedding for a low mass-damped hydroelastically mounted cylinder allowed to oscillate in the transverse direction. However the research of Blackburn et al. (2001) reveal that two-dimensional low Reynolds number simulations are insufficient to capture 2P shedding branches as these shedding modes appear to be strongly influenced by three-dimensional effects.
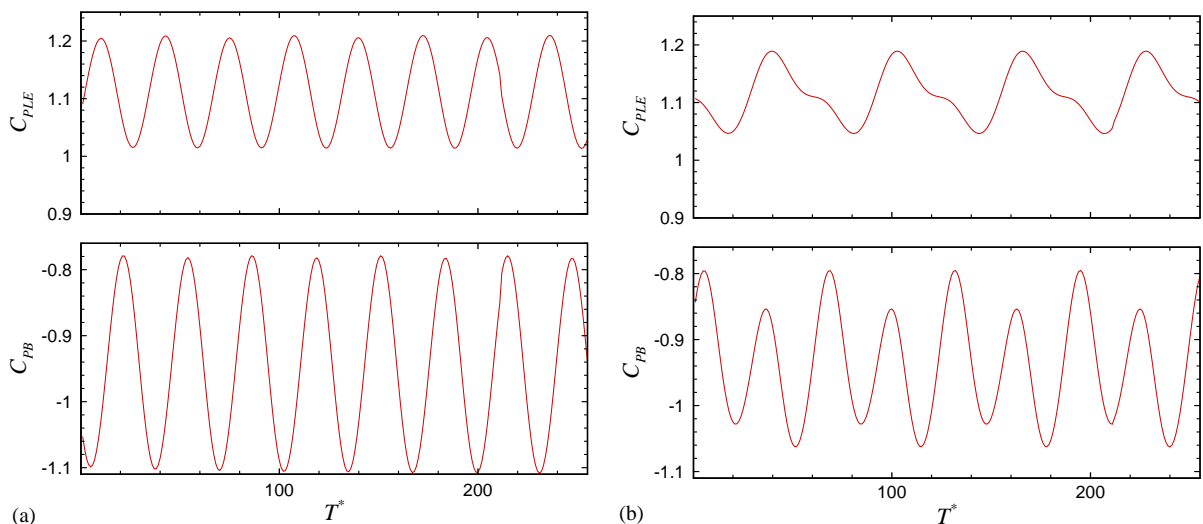

Fig. 13. (a) (Top) leading edge stagnation point pressure coefficient (C_{PLE}) and (bottom) base pressure coefficient (C_{PB}) as a function of normalized time, for $u^* = 2.5$. (b) (Top) leading edge stagnation point pressure coefficient (C_{PLE}) and (bottom) base pressure coefficient (C_{PB}) as a function of normalized time, for $u^* = 5.5$.

4.6. Predictions of the St_1 component in the drag response

The influence of the cylinder velocity on the calculated drag force over one cycle of oscillation was determined for $u^* = 5.5$, where the cylinder oscillations may be considered in-line with the flow direction.

In the reduced velocity range $u^* = 5.5$–19, the cylinder oscillation provides a variation in the flow field velocity with respect to the cylinder and hence an effective change in the local Reynolds number, that is, the Reynolds number based on the flow relative to the cylinder. The maximum local Reynolds number occurs at the point in the oscillation cycle where the cylinder is moving upstream with the greatest velocity. The minimum local Reynolds number occurs when the cylinder is moving downstream with the greatest velocity. The calculated maximum and minimum local Reynolds numbers at $u^* = 5.5$ were found to be $Re_{max} = 205.4$ and $Re_{min} = 194.7$, respectively. From the relationship between the Reynolds number and the drag coefficient, C_D, determined by Henderson (1995), this implies a maximum variation in the drag coefficient of 0.003 over one cycle. Therefore the drag coefficient may be considered effectively constant over a cycle of oscillation for $u^* = 5.5$. However, even though the drag coefficient is approximately constant, the drag force may vary substantially. The maximum drag force corresponds to the maximum local Reynolds number and the minimum drag force corresponds to the minimum local Reynolds number.

For all the reduced velocities considered in this study, the drag force acting on the cylinder is $180°$ out-of-phase with the cylinder velocity. Combining this with the definition of the drag coefficient, the ratio of maximum drag coefficient to minimum drag coefficient may be written as

$$\frac{C_{D_{max}}}{C_{D_{min}}} = \left[\frac{Re_{max}^2}{Re_{min}^2}\right] F_{D_{ratio}} \simeq 1. \tag{18}$$
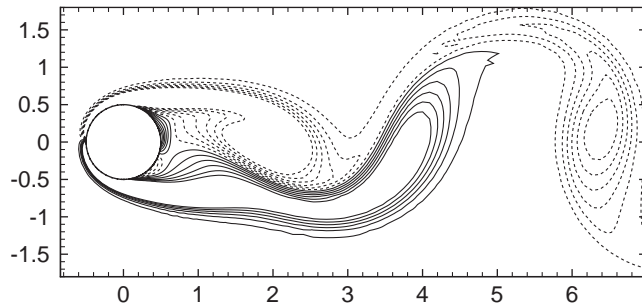

Fig. 14. Typical snapshot of the vorticity flow field for a tethered cylinder oscillating at a reduced velocity $u^* = 22$ at the top of its oscillation cycle.
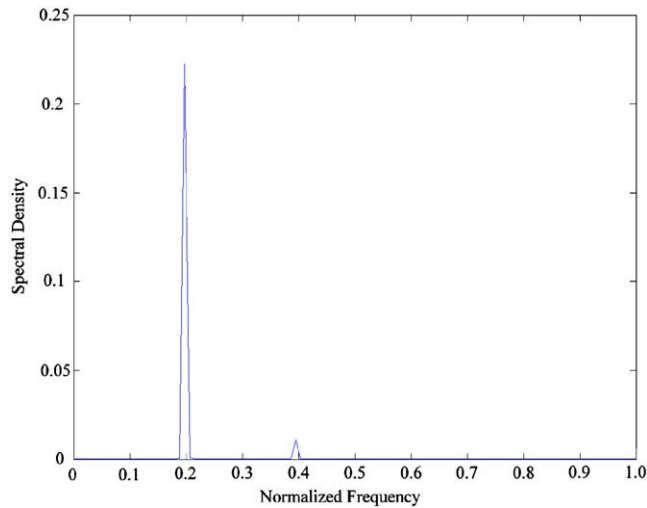

Fig. 15. Spectral density of the drag force for $u^* = 5.5$.

Here $F_{D_{\text{ratio}}} = F_{D_{\max}}/F_{D_{\min}}$ is the ratio of maximum to minimum drag force acting on the cylinder. Since the drag coefficient varies little over this Reynolds number range, Eq. (18) can be rearranged as

$$F_{D_{\text{ratio}}} = \frac{\text{Re}_{\min}^2}{\text{Re}_{\max}^2}. \tag{19}$$

For $u^* = 5.5$, the drag ratio was $F_{D_{\text{ratio}}} = 1.107$. By substituting this, and the values for the maximum and minimum Reynolds number quoted earlier into Eq. (19), we see that the variation in effective Reynolds number accounts for 81% of the observed variation in the drag ratio. The remainder is due to nonlinear effects including the Karman type wake shedding. To confirm this result, the spectral density of the drag is presented in Fig. 15. Two peaks are observed, occurring at St_1 and St_2. The larger of the two peaks, St_1, is due to the cylinder oscillation, and accounts for 82% of the energy in the drag trace, in close agreement with the predictions made above.

5. Conclusions

Two-dimensional simulations of the flow past a tethered cylinder have been performed for the reduced velocity range, $u^* = 1$–22, for a cylinder mass ratio $m^* = 0.833$. In this range of u^*, three distinct branches have been identified. The first branch, peaking at $u^* = 2.5$, is essentially an in-line branch and is driven by a resonance between the in-line forces and the natural frequency of the cylinder system. The second branch, occurring over the range $u^* = 5$–19, is initiated in the range $u^* = 3.5$–5 by resonance between the natural frequency of the tethered body system and the subharmonic of the drag force which peaks at $u^* = 5$. At higher reduced velocities, the motion of the cylinder modifies the drag response, such that the drag and lift have the same dominant frequency and are in-phase. The cylinder oscillates at the drag/lift frequency over the extent of the second branch. The motion of the cylinder alters the frequency of the leading-edge stagnation pressure, and as a result, alters the drag signal, such that the drag signal is dominated by the lift frequency, and both the drag and lift are in-phase. The third branch occurs for $u^* > 19$ and is dominated by transverse oscillations. The cylinder response for this branch is similar to that observed by Govardhan and Williamson (2000) for a low mass-damped hydroelastically mounted cylinder oscillating transverse to the flow field, as the cylinder oscillations reduce dramatically with increasing u^*, and the oscillations are no longer synchronized at the vortex shedding frequency from a fixed cylinder.

References

Angrilli, F., Di Silvo, G., Zanardo, A., 1974. Hydro-elastically study of a circular cylinder in a water stream. In: Naudascher, E. (Ed.)., Flow-Induced Structural Vibrations. Springer, Berlin.

Bearman, P., 1984. Vortex shedding from oscillating bluff bodies. Annual Review of Fluid Mechanics 16, 195–222.

Blackburn, H.M., Henderson, R.D., 1999. A study of two-dimensional flow past an oscillating cylinder. Journal of Fluid Mechanics 385, 255–286.

Blackburn, H.M., Govardhan, R., Williamson, C., 2001. A complementary numerical and physical investigation of vortex-induced vibration. Journal of Fluids and Structures 15, 481–488.

Feng, C., 1968. The measurements of vortex-induced vibrations of a long flexible circular cylinder. Master's thesis, University of British Columbia, Vancouver, Canada.

Govardhan, R., Williamson, C., 1997. Vortex-induced motions of a tethered sphere. Journal of Wind Engineering 69-71, 375–385.

Govardhan, R., Williamson, C., 2000. Modes of vortex formation and frequency response of a freely vibrating cylinder. Journal of Fluid Mechanics 420, 85–130.

Govardhan, R., Williamson, C., 2003. Resonance forever: existence of a critical mass and an infinite regime of resonance in votex-induced vibration. Journal of Fluid Mechanics 473, 147–166.

Harlemann, D., Shapiro, W., 1961. The dynamics of a submerged moored sphere in oscillatory waves. Coastal Engineering 2, 746–765.

Henderson, R., 1995. Details of the drag curve near the onset of vortex shedding. Physics of Fluids 7, 2102–2104.

Jauvtis, N., Govardhan, R., Williamson, C., 2001. Multiple modes of vortex-induced vibration of a sphere. Journal of Fluids and Structures 15, 555–563.

Karniadakis, G., Israeli, M., Orszag, S., 1991. High-order splitting methods of the incompressible Navier–Stokes equations. Journal of Computational Physics 97, 414–443.

Khalak, A., Williamson, C., 1999. Motions, forces and mode transitions in vortex-induced vibrations at low mass-damping. Journal of Fluids and Structures 13, 813–851.

King, R., 1974. Vortex excited oscillations of a circular cylinder in steady currents. In: Proceedings of the Offshore Technology Conference, OTC 1948, Houston, TX, USA.

Koopman, G., 1967. The vortex wakes of vibrating cylinders at low Reynolds numbers. Journal of Fluid Mechanics 28, 501–512.

Ogihara, K., 1988. Theoretical analysis on the transverse motion of a buoy by a surface wave. Applied Ocean Research 2, 51–56.

Parkinson, G., 1989. Phenomena and modelling of flow-induced vibrations of bluff bodies. Progress in Aerospace Sciences 26, 169–224.

Shi-Igai, H., Kono, T., 1969. Study on vibration of submerged spheres caused by surface waves. Coastal Engineering Japan 12, 29–40.

Shiels, D., Leonard, A., Roshko, A., 2001. Flow-induced vibration of a circular cylinder at limiting structural parameters. Journal of Fluids and Structures 15, 3–21.

Williamson, C., 1996. Three-dimensional wake transition. Journal of Fluid Mechanics 328, 345–407.

Williamson, C., Govardhan, R., 1997. Dynamics and forcing of a tethered sphere in a fluid flow. Journal of Fluids and Structures 11, 293–305.

Zhang, J., Dalton, C., 1998. A three-dimensional simulation of a steady approach flow past a circular cylinder at low Reynolds number. International Journal for Numerical Methods in Fluids 26, 1003–1022.